

A SUBMILLIMETER PERSPECTIVE ON THE GOODS FIELDS—II. THE HIGH RADIO POWER POPULATION IN THE GOODS-N^{1,2,3,4}

A. J. BARGER^{5,6,7}, L. L. COWIE⁷, F. N. OWEN⁸, L.-Y. HSU⁷, W.-H. WANG⁹

ApJ, 835, 95 (2017)

ABSTRACT

We use ultradeep 20 cm data from the Karl G. Jansky Very Large Array and 850 μ m data from SCUBA-2 and the Submillimeter Array of an 124 arcmin² region of the *Chandra* Deep Field-north to analyze the high radio power ($P_{20\text{ cm}} > 10^{31} \text{ erg s}^{-1} \text{ Hz}^{-1}$) population. We find that 20 (42 \pm 9%) of the spectroscopically identified $z > 0.8$ sources have consistent star formation rates (SFRs) inferred from both submillimeter and radio observations, while the remaining sources have lower (mostly undetected) submillimeter fluxes, suggesting that active galactic nucleus (AGN) activity dominates the radio power in these sources. We develop a classification scheme based on the ratio of submillimeter flux to radio power versus radio power and find that it agrees with AGN and star-forming galaxy classifications from Very Long Baseline Interferometry. Our results provide support for an extremely rapid drop in the number of high SFR galaxies above about a thousand solar masses per year (Kroupa initial mass function) and for the locally determined relation between X-ray luminosity and radio power for star-forming galaxies applying at high redshifts and high radio powers. We measure far-infrared (FIR) luminosities and find that some AGNs lie on the FIR-radio correlation, while others scatter below. The AGNs that lie on the correlation appear to do so based on their emission from the AGN torus. We measure a median radio size of $1''.0 \pm 0.3$ for the star-forming galaxies. The radio sizes of the star-forming galaxies are generally larger than those of the AGNs.

Subject headings: cosmology: observations — galaxies: distances and redshifts — galaxies: evolution — galaxies: starburst

1. INTRODUCTION

The local 20 cm population may be roughly divided into primarily star-forming galaxies at low radio power and primarily active galactic nucleus (AGN) dominated galaxies at high radio power (e.g., Condon 1989; Sadler et al. 2002; Mauch & Sadler 2007; Best & Heckman 2012). Such separations by galaxy type are mostly based on spectroscopic identifications. However, as we move to

¹ The James Clerk Maxwell Telescope is operated by the East Asian Observatory on behalf of The National Astronomical Observatory of Japan, Academia Sinica Institute of Astronomy and Astrophysics, the Korea Astronomy and Space Science Institute, the National Astronomical Observatories of China and the Chinese Academy of Sciences (Grant No. XDB09000000), with additional funding support from the Science and Technology Facilities Council of the United Kingdom and participating universities in the United Kingdom and Canada.

² The National Radio Astronomy Observatory is a facility of the National Science Foundation operated under cooperative agreement by Associated Universities, Inc.

³ The Submillimeter Array is a joint project between the Smithsonian Astrophysical Observatory and the Academia Sinica Institute of Astronomy and Astrophysics and is funded by the Smithsonian Institution and the Academia Sinica.

⁴ The W. M. Keck Observatory is operated as a scientific partnership among the California Institute of Technology, the University of California, and NASA, and was made possible by the generous financial support of the W. M. Keck Foundation.

⁵ Department of Astronomy, University of Wisconsin-Madison, 475 N. Charter Street, Madison, WI 53706, USA

⁶ Department of Physics and Astronomy, University of Hawaii, 2505 Correa Road, Honolulu, HI 96822, USA

⁷ Institute for Astronomy, University of Hawaii, 2680 Woodlawn Drive, Honolulu, HI 96822, USA

⁸ National Radio Astronomy Observatory, P.O. Box O, Socorro, NM 87801, USA

⁹ Academia Sinica Institute of Astronomy and Astrophysics, P.O. Box 23-141, Taipei 10617, Taiwan

higher redshifts, many of the radio sources become too faint for spectroscopic identifications. For example, in Barger et al. (2014), we found that an extended tail of microJansky radio sources with faint near-infrared (NIR) counterparts ($K_S > 22.5$) make up $\sim 30\%$ of the 20 cm population in the extremely deep (11.5 μ Jy at 5 σ) Karl G. Jansky Very Large Array (VLA) image (F. Owen 2017, in preparation) of the *Chandra* Deep Field-north (CDF-N; Alexander et al. 2003). To complicate matters, at high redshifts there are many more galaxies with extreme star formation rates (SFRs). Thus, the high radio power population begins to contain a significant fraction of star-forming galaxies, as well as continuing to be populated by numerous AGNs, resulting in a complex function with redshift of these competing processes (e.g., Cowie et al. 2004a).

In this paper, we develop a method to separate star-forming galaxies—galaxies where the SFRs inferred from the submillimeter observations are consistent with those inferred from the radio power—from AGNs in the high radio power population using a combination of ultradeep 20 cm and 850 μ m observations of the CDF-N. Long-wavelength submillimeter observations provide a clean discrimination between AGNs, whose spectral energy distributions (SEDs) drop extremely rapidly above a rest-frame wavelength of about 100 μ m (e.g., Mullaney et al. 2011), and galaxies dominated by star formation, whose graybody emission extends smoothly to the submillimeter. Both radio-quiet AGNs and star-forming galaxies can lie on the well-known FIR (8 – 1000 μ m)-radio correlation; however, because of their very different long-wavelength properties, they can be distinguished using the present technique. We then compare

our classifications with Very Long Baseline Interferometry (VLBI) classifications and with the X-ray properties of the sources.

Although submillimeter observations provide a valuable means of picking out extreme star formers in the high radio power population, observing large areas to any significant depth in the submillimeter is very difficult. Thus, we conclude by looking for a simpler diagnostic for separating star-forming galaxies from AGNs based on the radio data alone, namely, the radio size.

Our primary science goals are (1) to look for evidence of a characteristic maximum SFR for galaxies, as proposed by Karim et al. (2013) and Barger et al. (2014), (2) to determine whether locally determined relations between X-ray luminosity and radio power for star-forming galaxies apply at high redshifts and high radio powers, (3) to find whether AGNs in the high-redshift, high radio power population lie on the FIR-radio correlation (de Jong et al. 1985; Helou et al. 1985), as has been observed locally (Condon 1992; Morié et al. 2010; Wong et al. 2016), and (4) to examine whether any AGNs that lie on the correlation are there because star formation in the host galaxy is driving the observed radio emission, as proposed by Condon et al. (2013).

In Section 2, we present the radio, submillimeter, X-ray, and spectroscopic and photometric redshift data sets that we use in our analysis. In Section 3, we develop our classification method using the ratio of submillimeter flux to radio power and we compare our classifications of the high radio power sources with those made using radio-excess measurements, VLBI, and X-rays. In Section 4, we measure the FIR luminosities for the high radio power sources and determine their locations on a FIR luminosity versus radio power plot. We then construct SEDs for the star-forming galaxies and for the AGNs separately and determine whether they are consistent with the idea that star formation in the host galaxies is responsible for putting some AGNs on the FIR-radio correlation. Finally, in Section 5, we explore whether the separation between star-forming galaxies and AGNs could be done from radio sizes alone.

We assume the Wilkinson Microwave Anisotropy Probe cosmology of $H_0 = 70.5 \text{ km s}^{-1} \text{ Mpc}^{-1}$, $\Omega_M = 0.27$, and $\Omega_\Lambda = 0.73$ (Larson et al. 2011) throughout.

2. DATA

2.1. Radio and Submillimeter

We use ultradeep radio and submillimeter observations of the GOODS-N/CDF-N. The radio data are the ultradeep 20 cm image obtained in a 40 hr integration using the upgraded VLA in *A*-configuration (F. Owen 2017, in preparation). The image covers a 40' diameter with an effective resolution of 1''.8. The highest sensitivity region is about 9' in radius. The image probes to a 1σ limit of $2.3 \mu\text{Jy}$, making it the deepest radio image currently available at this wavelength. The absolute radio positions are known to 0''.1–0''.2 rms. We detect 445 radio sources above a 5σ threshold in the selected 124 arcmin² SCUBA-2 area. Of these, 210 are spatially resolved in the radio image. We measured sizes for these resolved sources and upper limits for the remaining sources.

The submillimeter data consist of an 101 hr 850 μm image that we obtained with SCUBA-2 (Holland et al.

2013) on the 15 m James Clerk Maxwell Telescope, together with follow-up high-resolution observations that we made with the Submillimeter Array (SMA; Ho et al. 2004). The center of the SCUBA-2 image has an rms depth of 0.28 mJy. In this paper, we consider an area of 124 arcmin² where the rms is less than 0.57 mJy (twice the central noise). For a detailed description of the reduction and calibration of SCUBA-2 data in general, we refer the reader to Chapin et al. (2013) and Dempsey et al. (2013). For specific details on the SCUBA-2 CDF-N image data reduction and calibration, we refer the reader to Chen et al. (2013) and Cowie et al. (2016).

We formed a matched filter image by weighting the SCUBA-2 image with the point spread function (PSF). This provides an optimal estimate of the flux at any position provided that, as expected, the sources are small compared with the beam full width half maximum (FWHM) of 14'' at 850 μm . We used a wider filter to subtract variable backgrounds so that the average measured flux at random positions in the image equals zero. We detect 115 sources at $> 4\sigma$ in the 124 arcmin² area. Of these, 41 have fluxes above 2.85 mJy, which is the flux threshold corresponding to a $> 5\sigma$ detection throughout the area.

Our SMA follow-up observations, together with archival data, give detections and high-precision subarcsecond positions for 22 submillimeter sources in this area, including all eight SCUBA-2 sources with fluxes above 6 mJy. Catalogs and further details on the SCUBA-2 image and the SMA data may be found in Cowie et al. (2016). Barger et al. (2014, 2015) used a substantial subset of the CDF-N SCUBA-2 data, as well as the SMA data, in their analyses.

In measuring the 850 μm fluxes for the radio sources without SMA counterparts, we first removed all of the detected SMA sources from the matched filter SCUBA-2 image using a PSF based on the observed calibrators. This left residual images from which we measured the 850 μm fluxes (whether positive or negative) and statistical errors at the radio positions. This procedure minimizes contamination by brighter submillimeter sources in the field.

2.2. X-Ray

The X-ray data are the 2 Ms X-ray image of Alexander et al. (2003), which they aligned with the Richards (2000) radio image. Near the aim point, the X-ray catalog reaches a limiting flux of $f_{0.5-2 \text{ keV}} \approx 1.5 \times 10^{-17} \text{ erg cm}^{-2} \text{ s}^{-1}$. Matching X-ray counterparts from the Alexander et al. (2003) catalogs to the radio sources is not critically dependent on the choice of match radius, as can be seen from Figure 7 of Alexander et al. (2003), which shows the positional offset between the X-ray and radio sources versus off-axis angle. Following Barger et al. (2007), we use a 1''.5 search radius. Of the radio sources in the CDF-N sample, 142 have X-ray counterparts. (There are a further 138 X-ray sources in the region that do not have radio counterparts.) When a radio source does not have an X-ray counterpart in the catalog, we measure the X-ray counts at the radio position from the X-ray image using a 3'' diameter and convert them to fluxes assuming a fixed photon index of $\Gamma = 1.8$. For all the sources, we compute the rest-frame 2 – 8 keV luminosities, L_X , from the 0.5 – 2 keV fluxes

with no absorption correction and $\Gamma = 1.8$ using

$$L_X = 4\pi d_L^2 f_{0.5-2\text{ keV}} ((1+z)/4)^{\Gamma-2} \text{ erg s}^{-1}. \quad (1)$$

We take $L_X > 10^{44} \text{ erg s}^{-1}$ as the threshold for a source to be classified as an X-ray quasar.

2.3. Redshifts

There is a large amount of ancillary data on the CDF-N. However, the most important information for this analysis is the spectroscopic data. Here we draw on a new compilation of known spectroscopic redshifts in the region (A. Barger et al. 2017, in preparation; see also Cohen et al. 2000; Cowie et al. 2004b, 2016; Swinbank et al. 2004; Wirth et al. 2004, 2015; Chapman et al. 2005; Reddy et al. 2006; Trouille et al. 2008; Barger et al. 2008; Cooper et al. 2011), the bulk of which come from Keck spectroscopy with DEIMOS, LRIS, and MOSFIRE. The compilation includes redshifts based on our own analysis of the HST grism data on the GOODS-N (PI: B. Weiner; Momcheva et al. 2016), but this only adds one redshift which is not identified otherwise.

Of the 445 radio sources in the 124 arcmin² area, 343 (77%) have spectroscopic redshifts. These include a small number of CO spectroscopic redshifts from Daddi et al. (2009a,b), Bothwell et al. (2013), and Walter et al. (2012). We use photometric redshifts from Rafferty et al. (2011) to augment the spectroscopic redshifts, which raises the redshift identifications to 392. The remaining 53 radio sources are very faint in the optical and NIR with median z -band magnitudes of 26.2 and median K_S -band magnitudes of 23.1.

2.4. High Radio Power Sources

For all of the sources with either spectroscopic or photometric redshifts, we compute the rest-frame radio power using the equation

$$P_{20\text{ cm}} = 4\pi d_L^2 f_{20\text{ cm}} 10^{-20} (1+z)^{\alpha-1} \text{ erg s}^{-1} \text{ Hz}^{-1}, \quad (2)$$

where d_L is the luminosity distance (cm) and $f_{20\text{ cm}}$ is the 20 cm flux in units of μJy . This equation assumes $S_\nu \propto \nu^{-\alpha}$, where we adopt a radio spectral index of $\alpha = 0.8$ (Condon 1992; Ibar et al. 2010). The choice of α may not be appropriate for AGNs and also may be problematic for high-redshift sources. However, it should be accurate enough for the present purposes.

There are 46 high radio power sources (defined here as $P_{20\text{ cm}} > 10^{31} \text{ erg s}^{-1} \text{ Hz}^{-1}$) with spectroscopic or photometric redshifts in the 124 arcmin² area. All of these lie at $z > 0.8$. The lowest redshift is $z = 0.847$, and the highest redshift is $z = 5.18$ (see Figure 1). We return to the sources with no redshift identifications at the end of Section 3.

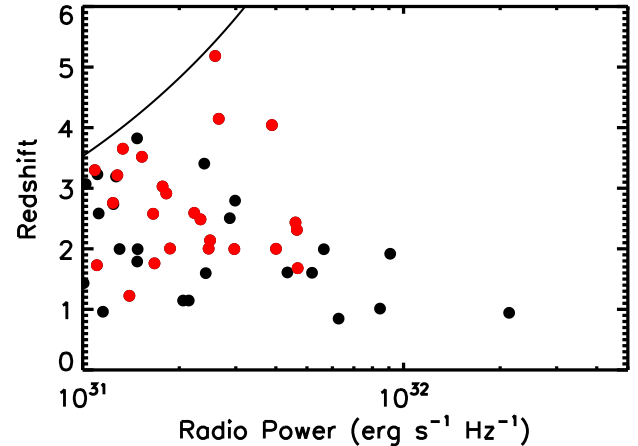


FIG. 1.— Redshift vs. radio power. The detection threshold for the radio sample is shown with the black curve. Red circles show sources detected above the 3σ level at $850 \mu\text{m}$, while black circles show sources not detected at this level.

In Figure 1, we show the distribution of redshifts versus radio power, distinguishing sources with submillimeter detections ($> 3\sigma$; red circles) from those without (black circles). Most of the sources lie in the redshift range $z = 1 - 3$. The spectroscopic and photometric redshift measurements may introduce biases in the identifications. In particular, the highest redshift ($z > 4$) sources are all based on CO measurements; thus, all are submillimeter-detected sources. However, this does not affect our analysis, since we compare only identified sources, and such a comparison does not depend on the completeness of the sample.

2.5. The FIR-radio Correlation

The local FIR-radio correlation (de Jong et al. 1985; Helou et al. 1985) is well characterized by a linear fit over five orders of magnitude. It is parameterized by the quantity

$$q = \log \left(\frac{L_{8-1000 \mu\text{m}}}{3.75 \times 10^{12} \text{ erg s}^{-1}} \right) - \log \left(\frac{P_{20 \text{ cm}}}{\text{erg s}^{-1} \text{ Hz}^{-1}} \right). \quad (3)$$

The average local value is $q = 2.52 \pm 0.01$ for an $8 - 1000 \mu\text{m}$ luminosity (Yun et al 2001; this is after applying their correction of 1.5 from their measured $42.5 - 122.5 \mu\text{m}$ luminosity; see also Bell 2003). This is very similar to the values measured at high redshifts from submillimeter samples with accurate positions from submillimeter interferometric observations (e.g., average $q = 2.51 \pm 0.01$, Barger et al. 2012; median $q = 2.56 \pm 0.05$, Thomson et al. 2014).

3. STAR-FORMING GALAXIES VERSUS AGNS

Barger et al. (2014) noticed in their plot of $850 \mu\text{m}$ flux (their $850 \mu\text{m}$ rms error was $< 1.5 \text{ mJy}$) versus radio power that submillimeter-detected ($> 4\sigma$) radio sources (submillimeter-bright) bifurcate from other radio sources (submillimeter-blank) above $P_{20 \text{ cm}} \approx 10^{31} \text{ erg s}^{-1} \text{ Hz}^{-1}$. Based on a small number (5) of such sources that also had high-resolution radio observations (Chapman et al. 2004; Muxlow et al. 2005; Momjian et al. 2010; Guidetti et al. 2013), Barger et al. found that the submillimeter-bright sources appeared to be extended and star-formation

dominated, while the submillimeter-blank sources appeared to be compact.

Here we explore this observed bifurcation further using our deeper submillimeter data. In Figure 2, we plot 850 μm flux versus radio power for the high radio power sources with spectroscopic or photometric redshifts (black circles). Because the negative K -correction in the FIR/submillimeter closely offsets the dimming effects of distance for $z > 1$ (Blain et al. 2002; Casey et al. 2014), the observed-frame submillimeter flux is a proxy for FIR luminosity for star-forming galaxies. (Note that the precise conversion of submillimeter flux to FIR luminosity depends on the SED of the galaxy.) Thus, we can compare the submillimeter flux with the 20 cm power, which should also measure the SFR if it is dominated by diffuse synchrotron emission produced by relativistic electrons accelerated in supernovae remnants. We denote the sources that also have SMA detections with blue circles. Using Equation 3, we also plot submillimeter flux versus radio power (blue curve) assuming $q = 2.52$ and adopting the mean conversion

$$\log L_{8-1000 \mu\text{m}} (\text{erg s}^{-1}) = \log S_{850 \mu\text{m}} (\text{mJy}) + 45.60 \pm 0.05 \quad (4)$$

determined by Cowie et al. (2016; their Equation 3, which was based on 26 SCUBA-2 galaxies in the *GOODS-Herschel* (Elbaz et al. 2011) region with accurate positions and spectroscopic redshifts).

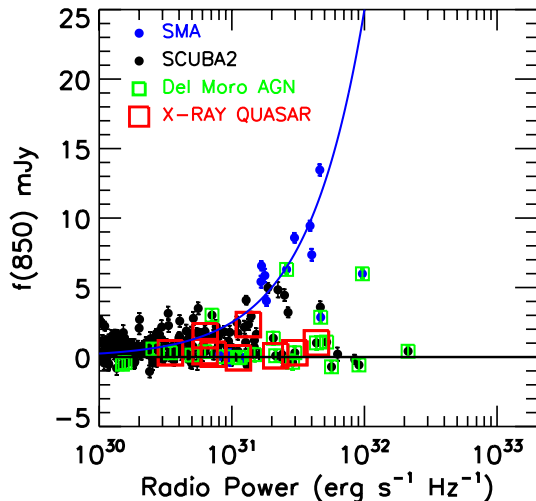


FIG. 2.— 850 μm flux vs. 20 cm power for the radio sources with spectroscopic or photometric redshifts. All submillimeter fluxes are from the SCUBA-2 image. Sources that also have SMA detections are shown as blue circles, while the other SCUBA-2 measurements are shown as black circles. All of the SMA flux measurements are consistent with the SCUBA-2 fluxes within the errors. Error bars are $\pm 1\sigma$. The blue curve shows submillimeter flux vs. radio power based on Equations (3) and (4) and assuming $q = 2.52$. Sources identified as radio excess by Del Moro et al. (2013) are shown with enclosing green squares, while X-ray quasars are shown with enclosing red squares.

The bifurcation between submillimeter-bright (star-forming galaxies) and submillimeter-blank (AGNs) is clear, with only a few sources lying in a region that may indicate they are composites (where the radio power has contributions from both star formation and AGN ac-

tivity). We mark with enclosing red squares the X-ray quasars in the field, all of which lie on the submillimeter-blank track.

Before proceeding to a comparison of our classifications with radio-excess, VLBI, and X-ray classifications, it is important to note that our analysis does not include the radio sources without spectroscopic or photometric redshifts in the area. These sources are faint in the optical and NIR. Based on the $K - z$ relation, they are likely to lie at high redshifts (Barger et al. 2014). The higher redshifts (which shifts emission lines out of the observable spectral range) and faintness make them hard to identify with optical and NIR spectroscopy. However, they appear to contain a similar fraction of submillimeter galaxies as the high radio power sources with redshifts; 34 \pm 9% of those without redshifts have 850 μm detections above a 3σ threshold, compared to 46 \pm 9% of those with redshifts and a radio power above $10^{31} \text{ erg s}^{-1} \text{ Hz}^{-1}$. Thus, while the unidentified sources may comprise the higher redshift tail of the high radio power sample, the submillimeter detections suggest they may be similar to the identified sources in other regards.

3.1. Radio Excess

Del Moro et al. (2013) looked for radio-excess candidates—those with excess radio emission over that expected from star formation processes and hence likely to host AGN activity—in a 24 μm detected sample with $> 3\sigma$ 20 cm flux measurements (their VLA/24 μm sample). The 20 cm fluxes were measured from the CDF-N radio image of Morrison et al. (2010; rms noise level of $\sim 3.9 \mu\text{Jy}$) at the positions of the 24 μm sources (which are the same as the positions of the 3.6 μm sources, since the IRAC 3.6 μm sources were used as priors). They performed a detailed SED analysis of the 458 VLA/24 μm sources with $z \leq 3.0$ and then calculated the FIR flux by integrating the total SEDs over the rest-frame wavelength range $\lambda = 42.5 - 122.5 \mu\text{m}$. They defined radio-excess sources as having $q < 1.68$.

We examined their sample of 51 radio-excess candidates with our deeper VLA data and larger redshift catalog and found about one-quarter of them to be spurious. Most of the problems seemed to come from up-scattered sources in the noisier Morrison et al. (2010) 20 cm image being identified as radio-excess sources. The data from the upgraded VLA used in this work rule these candidates out, as well as one candidate that is part of a radio jet. Several other sources were allocated incorrect redshift identifications, including HDF850.1, which is at $z = 5.124$ (Walter et al. 2012) but was placed at the redshift of the neighboring elliptical galaxy. After removing the spurious sources, there are 37 radio-excess candidates left. In Figure 2, we show with enclosing green squares the radio-excess candidates that overlap with our sample. They mostly fall in the AGN regime, as expected, though one object is clearly a star-forming galaxy and several are composites.

3.2. VLBI

Next, we compare our classifications with those made from VLBI 20 cm observations. First, in Figure 3, we show the information presented in Figure 2 (but restricted to sources that match our high radio power definition of $P_{20 \text{ cm}} > 10^{31} \text{ erg s}^{-1} \text{ Hz}^{-1}$) as a ratio plot,

which allows us to illustrate the full dynamic range of the data. We plot the ratio of $850 \mu\text{m}$ flux to 20 cm power versus 20 cm power. We show the radio sources for which the submillimeter flux measurement at the radio position has a signal-to-noise ratio (S/N) $\geq 2\sigma$ as circles with 1σ uncertainties, and we show $\text{S/N} < 2\sigma$ as circles at the 2σ limit with downward pointing arrows. We use colors to denote the sources classified as either compact (Chi et al. 2013; cyan) or extended (Momjian et al. 2010; red) from VLBI data. Finally, we denote with green shading the factor of two range found by Barger et al. (2014) over which we expect the SFRs derived from the submillimeter fluxes to be consistent with the SFRs derived from the radio power, assuming the FIR-radio correlation with the radio emission dominantly powered by star formation. This multiplicative factor of two is the systematic error in the individual SFRs determined from the submillimeter fluxes based on the variations in their SEDs (see also Cowie et al. 2016).

All of the radio sources within the green shaded region have $\text{S/N} \geq 2\sigma$ submillimeter flux measurements, while only a handful of the radio sources that lie below the green shaded region have submillimeter flux measurements or upper limits that are well below what would be expected if the radio power were produced by star formation. Thus, the radio power in these sources must be dominated by AGN contributions. All of the VLBI compact sources lie below the green shaded region, while the one VLBI extended source lies within the green shaded region.

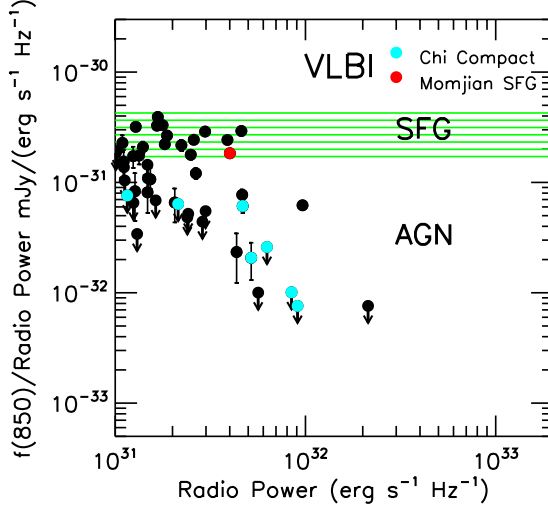


FIG. 3.— $850 \mu\text{m}$ flux/ 20 cm power vs. 20 cm power for the radio sources with spectroscopic or photometric redshifts and $P_{20 \text{ cm}} > 10^{31} \text{ erg s}^{-1} \text{ Hz}^{-1}$ (circles). Sources with $\text{S/N} \geq 2\sigma$ submillimeter flux measurements are shown with 1σ uncertainties, while those with $\text{S/N} < 2\sigma$ are shown at the 2σ limit with downward pointing arrows. The green shaded region shows where the submillimeter flux and radio power produce consistent estimates of the SFRs. Cyan and red circles show sources classified as AGNs and star-forming galaxies (SFGs), respectively, from VLBI observations.

Perhaps most striking, above $P_{20 \text{ cm}} \approx 5 \times 10^{31} \text{ erg s}^{-1} \text{ Hz}^{-1}$ there are no sources in the green shaded region, which is consistent with the claim by Karim et al. (2013) and Barger et al. (2014) that there

is a characteristic maximum SFR for star-forming galaxies above which the number of galaxies drops extremely rapidly. We note that although more luminous star-forming galaxies, such as the submillimeter galaxy GN20 (Pope et al. 2005; Daddi et al. 2009b), which lies just outside the 124 arcmin^2 area studied here, do exist, they are rare. GN20, which has $P_{20 \text{ cm}} = 7.5 \times 10^{31} \text{ erg s}^{-1} \text{ Hz}^{-1}$, is one of only two sources with $850 \mu\text{m}$ fluxes above 15 mJy in the more extended 400 arcmin^2 region of the CDF-N covered by the SCUBA-2 image to an rms of 1.5 mJy (Cowie et al. 2016). Based on the submillimeter number densities, the surface density of these more luminous star-forming galaxies with $P_{20 \text{ cm}} > 5 \times 10^{31} \text{ erg s}^{-1} \text{ Hz}^{-1}$ is about 0.01 times the surface density of star-forming galaxies with $P_{20 \text{ cm}} = (1 - 5) \times 10^{31} \text{ erg s}^{-1} \text{ Hz}^{-1}$ (the $\pm 1\sigma$ range is 0.006 to 0.037).

Hereafter, we classify the sources that lie inside the green shaded region as star-forming galaxies, the small number of sources that lie below that region but have $\geq 3\sigma$ submillimeter detections as composites, and the remaining sources as AGN dominated.

3.3. X-ray

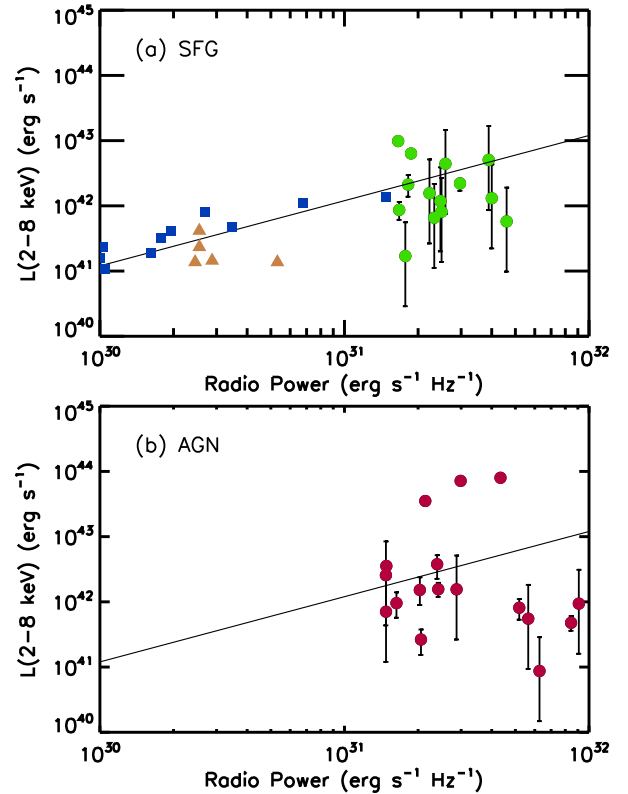


FIG. 4.— Rest-frame $2 - 8 \text{ keV}$ luminosity vs. radio power for the radio sources with spectroscopic or photometric redshifts and $P_{20 \text{ cm}} > 1.4 \times 10^{31} \text{ erg s}^{-1} \text{ Hz}^{-1}$ and either (a) consistent SFRs from the radio and submillimeter (green circles) or (b) not detected in the submillimeter (red circles). In (a), we also show the sample of local ULIRGs (gold triangles) and CDF-N star-forming galaxies with $z = 1 - 1.3$ (blue squares) from Mineo et al. (2014), together with their fit of the X-ray luminosity vs. radio power (black line).

We now compare our classifications with the X-ray properties of the sample. In Figure 4, we show rest-

frame 2–8 keV luminosity (computed from the observed-frame 0.5–2 keV flux, as described in Section 2.2, to take advantage of the higher sensitivity in this energy band) versus the 20 cm power for the radio sources with spectroscopic or photometric redshifts and $P_{20\text{ cm}} > 1.4 \times 10^{31} \text{ erg s}^{-1} \text{ Hz}^{-1}$. The use of the 0.5–2 keV flux to compute the 2–8 keV luminosity also minimizes any uncertainty in the K -corrections computed from the X-ray spectral slope with the relation being exact at $z = 3$. We chose this radio power threshold to provide a clean separation in Figure 3 between star-forming galaxies and AGNs.

At lower redshifts ($z < 1.3$) and radio powers, Mineo et al. (2014) compared X-ray luminosity with radio power for a sample of galaxies from the CDF fields that they considered to be star-formation dominated based on their colors and morphologies. In Figure 4(a), we show their CDF-N sample with $P_{20\text{ cm}} > 10^{30} \text{ erg s}^{-1} \text{ Hz}^{-1}$ (blue squares) after converting their 0.5–8 keV luminosities to 2–8 keV luminosities using a factor of 0.56. We also show their measurements for a sample of local ULIRGs (golden triangles). Mineo et al. fitted their data over four orders of magnitude in radio power with the linear relation

$$L_{2-8 \text{ keV}} (\text{erg s}^{-1}) = 1.2 \pm 0.1 \times 10^{11} P_{20\text{ cm}} (\text{erg Hz}^{-1}) \quad (5)$$

(black line in Figure 4). Lehmer et al. (2016) discuss the dependence of the Mineo et al. relation on the specific SFRs, but for very high specific SFRs, they reproduce the Mineo et al. equation, which should be appropriate for the present objects.

The X-ray luminosities of the star-forming galaxies in Figure 4(a) are consistent with an extrapolation of the Mineo et al. (2014) equation to higher radio powers. The mean 2–8 keV luminosity to radio power ratio of our star-forming galaxies is $1.22 \pm 0.43 \times 10^{11} \text{ Hz}$, where we have computed the error using the jackknife resampling statistic. This is almost identical to the Mineo et al. normalization, extending the applicability of their relation to galaxies with $\text{SFRs} > 1000 M_{\odot} \text{ yr}^{-1}$. The extremely high SFRs of the present sample result in some of the X-ray luminosities being even greater than the $L_{2-8 \text{ keV}} = 10^{42} \text{ erg s}^{-1}$ value often used to identify sources as clear AGNs (e.g., Hornschemeier et al. 2001; Barger et al. 2002; Bauer et al. 2004; Szokoly et al. 2004) based on maximal local star-forming galaxy X-ray luminosities. Laird et al. (2010) similarly concluded that very high SFRs were responsible for the high X-ray luminosities of most of the sources in their submillimeter-selected sample in the same field.

The AGN-classified sources in Figure 4(b) show a much wider spread in $L_{2-8 \text{ keV}}$, ranging from near quasar X-ray luminosities to nearly X-ray undetected sources. However, there are a number of sources with luminosities close to those of the star-forming galaxies, and there is clearly not a one-to-one correlation between our classifications and X-ray luminosity.

4. THE FIR-RADIO CORRELATION

Radio power is often used along with the FIR-radio correlation as a measure of the SFR (e.g., Cram et al. 1998; Hopkins et al. 2003; Netzer et al. 2007; Mushotzky et al. 2014; Mineo et al. 2014). However, this could be

risky when no other information is available on whether a source is AGN dominated or star-formation dominated. After all, it is well known that some local radio-quiet AGNs lie on the FIR-radio correlation (e.g., Condon 1992; Morić et al. 2010; Wong et al. 2016), even if it is not understood why.

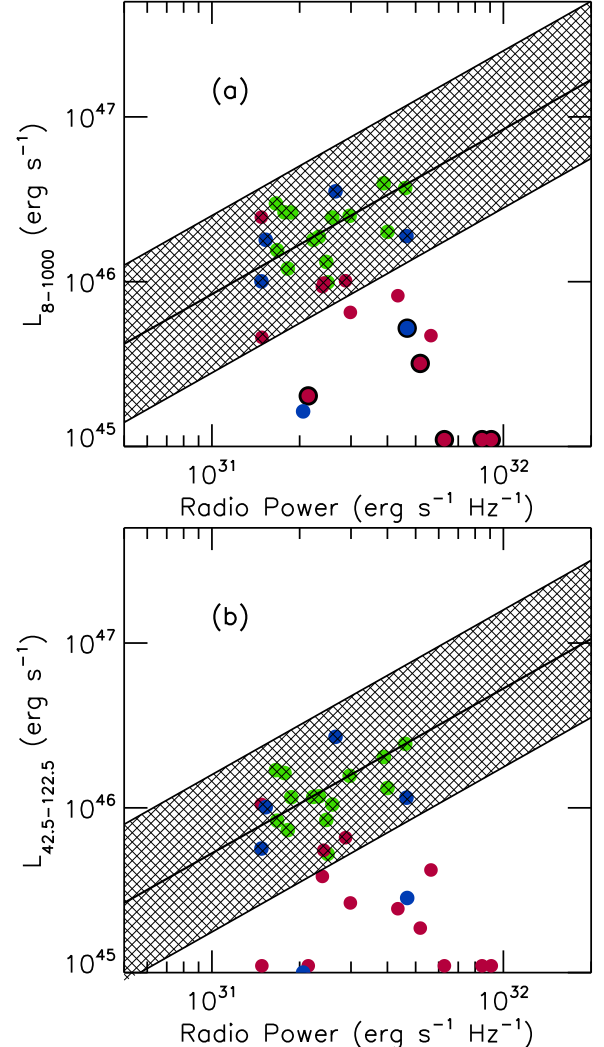


FIG. 5.— (a) $8 - 1000 \mu\text{m}$ luminosity and (b) $42.5 - 122.5 \mu\text{m}$ luminosity vs. 20 cm power for the radio sources with spectroscopic or photometric redshifts and $P_{20\text{ cm}} > 1.4 \times 10^{31} \text{ erg s}^{-1} \text{ Hz}^{-1}$. Green circles denote star-forming galaxies, blue circles composites, and red circles AGNs. The central black line shows the median FIR-radio correlation of the star-forming galaxies, and the shading shows the region where we consider the sources to lie on the FIR-radio correlation (multiplicative factor of 3 of the central value). In (a), we mark the sources that Chi et al. (2013) found to be AGNs using VLBI observations with surrounding black circles. All of these sources lie below the FIR-radio correlation.

In Figure 5, we plot (a) $8 - 1000 \mu\text{m}$ luminosity and (b) $42.5 - 122.5 \mu\text{m}$ luminosity versus radio power for the radio sources with spectroscopic or photometric redshifts and $P_{20\text{ cm}} > 1.4 \times 10^{31} \text{ erg s}^{-1} \text{ Hz}^{-1}$. We use colors to denote the sources classified as star-forming galaxies (green circles), composites (blue circles), and AGNs (red circles). In (a), we also mark the sources that Chi et al. (2013) found to be AGNs using VLBI observations with surrounding black circles. All of these sources lie below

the FIR-radio correlation. The star-forming galaxies in (a) have a mean $q = 2.42 \pm 0.06$, where we have computed the error with the jackknife resampling statistic; all lie within a multiplicative factor of three of the median value ($q = 2.35$), which we denote by shading. Five AGNs and four composites also lie in this region.

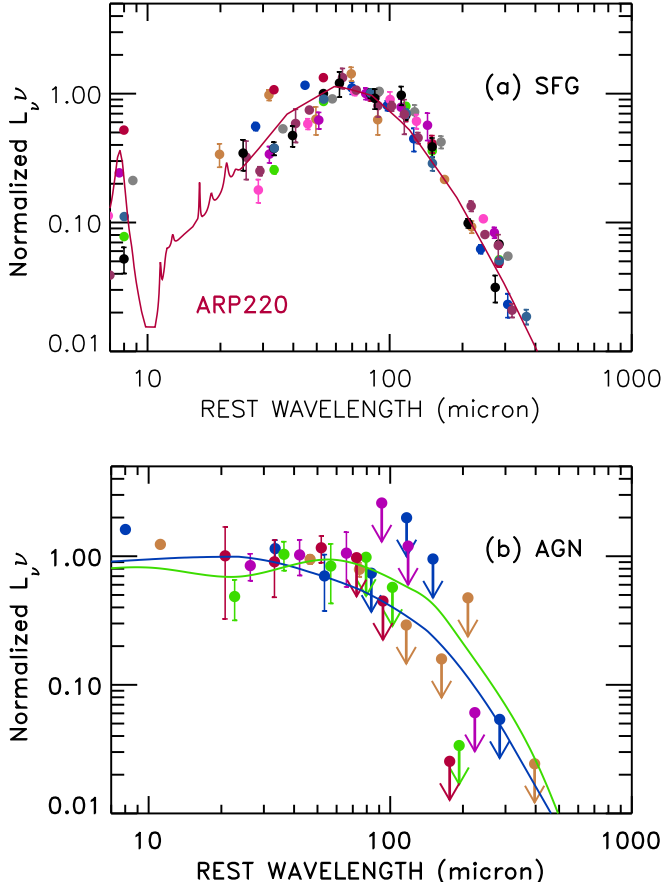


FIG. 6.— SEDs for the radio sources with spectroscopic or photometric redshifts and $P_{20 \text{ cm}} > 1.4 \times 10^{31} \text{ erg s}^{-1} \text{ Hz}^{-1}$ that lie on the FIR-radio correlation (i.e., the shaded region in Figure 5): (a) 12 star-forming galaxies (excluding the highest redshift HDF850.1 where the short wavelengths are poorly defined), and (b) 5 AGNs. The error bars are $\pm 1\sigma$. When a source is not detected at the 2σ level at a particular wavelength, we show it at the 2σ value with a downward pointing arrow. The star-forming galaxies in (a) show the characteristic shape of luminous starburst galaxies, which we illustrate using the Arp 220 SED from Silva et al. (1998) (red curve). The AGNs in (b) show a torus-dominated SED, which we illustrate using the SWIRE templates for type I quasars (blue curve) and type II quasars (green curve).

In Figure 6(a), we show the SEDs of 12 of the star-forming galaxies that lie on the FIR-radio correlation, as defined by the shaded region of Figure 5(a). We excluded the highest redshift source HDF850.1, because the short wavelength data are not well defined. These star-forming galaxies show the characteristic shape of luminous starburst galaxies, as we illustrate by superimposing the Arp 220 SED from Silva et al. (1998) (red curve).

In Figure 6(b), we show the five AGNs from Figure 5(a) that lie on the FIR-radio correlation. They show typical torus SEDs and are undetected at wavelengths $\gtrsim 60 \mu\text{m}$ in the rest frame. We superimpose the quasar type I (blue curve) and type II (green curve) templates from the

SWIRE template library¹⁰ (Polletta et al. 2006, 2007). Symeonidis et al. (2016) give a very similar SED for the type I quasars based on a carefully selected and analyzed sample.

The template quasar SEDs are broadly similar to our observations, though our observed SEDs appear to fall more sharply at the longer wavelengths. For these AGNs, the FIR luminosity and the radio power are not a measure of the SFR in the host galaxies. Indeed, the fact that these AGNs lie on the FIR-radio correlation seems to be a coincidence. From Figure 5(b), we see that when we use the $42.5 - 122.5 \mu\text{m}$ luminosity instead of the $8 - 1000 \mu\text{m}$ luminosity, the locations of the star-forming galaxies remain about the same, while the AGNs drop substantially.

5. RADIO SIZES

In previous work, radio morphologies and/or radio spectral indices have been used, together with mid-infrared (MIR) data, to pick out star-forming galaxies and then measure their radio sizes (Muxlow et al. 2005; Guidetti et al. 2013). Muxlow et al. found sizes from $0''.2 - 3''.0$ with a median size of $1''.0$. They also found that most of the AGNs were compact. In other work, radio sizes of submillimeter and millimeter selected galaxies have been measured (Chapman et al. 2004; Biggs & Ivison 2008; Miettinen et al. 2015). The advantage of the present data is that we can compare the radio sizes of the classified star-forming galaxies and AGNs in our purely radio selected sample without any selection dependence on the radio morphologies. We could, in principle, use the submillimeter sizes from the SMA data to carry out a similar exercise, but the resolution and signal-to-noise is too low for this to be useful.

In Figure 7, we show radio size versus the ratio of $850 \mu\text{m}$ flux to radio power for the $f_{20 \text{ cm}} > 40 \mu\text{Jy}$ sources with spectroscopic or photometric redshifts and $P_{20 \text{ cm}} > 1.4 \times 10^{31} \text{ erg s}^{-1} \text{ Hz}^{-1}$. We apply the radio flux limit to ensure high enough S/Ns for accurate deconvolution to be able to measure the radio sizes. This limit was based on model tests within the current data set. We show the unresolved sources with downward pointing arrows. We again use colors to denote the sources classified as star-forming galaxies (green), composites (blue), or AGNs (red). We use larger black circles to highlight the two double-lobed radio sources in our sample, which are very extended in the radio.

All but one of the star-forming galaxies are resolved in the 20 cm image, and all but one of the resolved star-forming galaxies have sizes in the rather narrow range $0''.42$ to $1''.36$ (physical sizes from 4 kpc to 12 kpc). The one larger source is the heavily studied source SMG123707+621408. This source has two separated components, each of which is individually similar to the remaining star-forming galaxies. However, since the CO map of Tacconi et al. (2006) appears to join the two components, we have used the full extent of the two components in measuring the radio size rather than splitting them. We note, however, that the submillimeter continuum flux arises from only one of the components. Deciding what size to allocate to such sources is difficult; fortunately, though, such sources are not common, with

¹⁰ [http://www.iasf-milano.inaf.it/\\$sim\\$polletta/templates/swiretemplates.html](http://www.iasf-milano.inaf.it/simpolletta/templates/swiretemplates.html)

only this one example lying in our observed region.

We show the distributions of the sizes in the AGN (top) and star-forming galaxy (bottom) populations in Figure 8, where we have put the unresolved sources in at the upper limits on their sizes (open portions of histograms). The median size of the star-forming galaxies is $1''.0 \pm 0.3$, while that of the AGNs (excluding the double-lobed sources) is $0''.45 \pm 0.05$. (The value of the AGNs drops to $0''.4$ if we put the unresolved sources in at zero.)

There are only two composites, one of which is unresolved. If we conservatively put the three unresolved AGNs at their upper limits and include both composites in a combined AGN/composite category (putting the unresolved composite at its upper limit), then the differences in the size distributions between the star-forming galaxies and the AGNs/composites are highly significant, with a Mann-Whitney test giving only a 0.002 probability (two sided) that the two distributions are consistent.

Even with the current 20 cm resolution, we can pick out most of the star-forming galaxies based on radio size and morphology. The double-lobed radio sources are easily classified as AGNs on the basis of radio morphology, while for the remaining sources, we find that choosing those that are resolved and greater than $0''.5$ (blue dotted line in Figure 7) would correctly classify the bulk of the star-forming galaxies, while avoiding contamination from the resolved AGNs. However, it should be noted that the most compact star-forming galaxies have sizes that are hard to distinguish from the AGNs using the present spatial resolution.

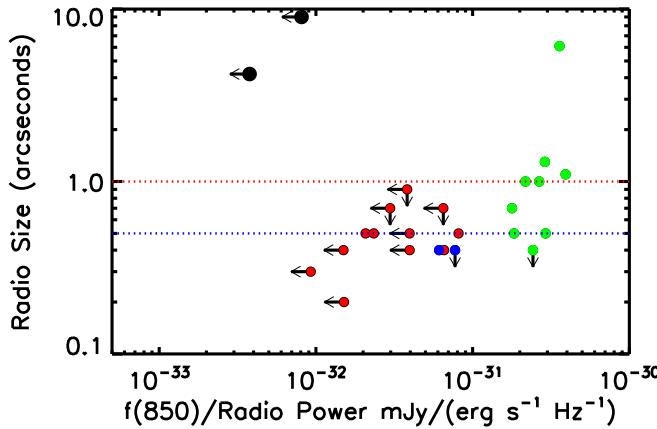


FIG. 7.— 20 cm size vs. the ratio of $850 \mu\text{m}$ flux to radio power for the $f_{20\text{cm}} > 40 \mu\text{Jy}$ sources with spectroscopic or photometric redshifts and $P_{20\text{cm}} > 1.4 \times 10^{31} \text{ erg s}^{-1} \text{ Hz}^{-1}$. Unresolved sources are shown with downward pointing arrows. Green circles denote star-forming galaxies, blue circles composites, and red circles AGNs. The larger black circles show the double-lobed radio sources in the field both classified as AGNs based on their radio morphology; these are very extended in the radio. The red dotted line shows the median size of the star-forming galaxies. The blue dotted line shows a dividing line of $0''.5$ that would correctly classify most of the resolved sources.

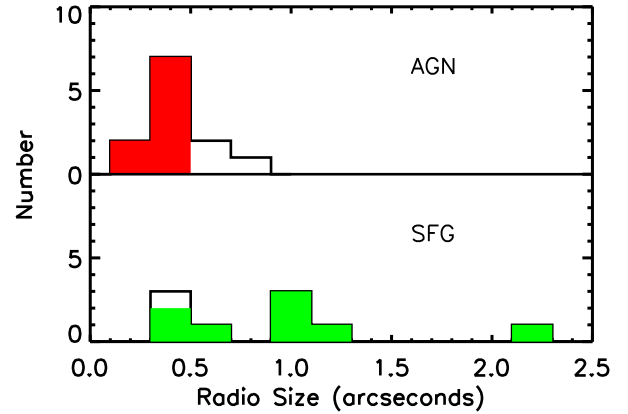


FIG. 8.— Histogram of 20 cm size for the $f_{20\text{cm}} > 40 \mu\text{Jy}$ sources with spectroscopic or photometric redshifts and $P_{20\text{cm}} > 1.4 \times 10^{31} \text{ erg s}^{-1} \text{ Hz}^{-1}$. These are separated into AGNs (top) and star-forming galaxies (bottom). The two double-lobed radio sources, which have large sizes, are not shown in the AGN panel. In the star-forming galaxy panel, the source SMG123707+621408 discussed in the text is shown at a nominal value of $2''.2$ to keep it on the plot. The colored histograms show sources with resolved sizes, and the open histograms show sources that are not resolved, put at the upper limits on their sizes. These sources could lie anywhere to the left.

The radio sizes for the star-forming galaxies are comparable to (though slightly larger than) the radio sizes measured for samples of galaxies with submillimeter detections by Chapman et al. (2004) ($0''.83 \pm 0.14$) and Biggs & Ivison (2008) ($0''.64 \pm 0.14$). However, all of these radio sizes are generally larger than those measured from submillimeter continuum observations (typically about $0''.3$; Simpson et al. 2015) by factors of 2 – 3. It is unclear what the explanation for this is when we have found here that the radio power is a good tracer of the FIR for the high radio power selected star-forming galaxy sample (see Figure 5). Simpson et al. suggest that it may be a consequence of cosmic ray diffusion, but they then argue that this is unlikely for the strong submillimeter galaxies. (See also Miettinen et al. 2015’s Section 6.3 for a discussion of this issue based on a comparison of their 10 cm sizes with the millimeter continuum sizes from Ikarashi et al. (2015).) The origin of the effect therefore remains to be determined.

6. SUMMARY

In this paper, we used ultradeep radio and submillimeter data on the GOODS-N/CDF-N to develop a classification method based on the ratio of the submillimeter flux to the radio power to separate star-forming galaxies from AGNs in the high radio power population. We found that our classifications agreed with classifications made from high-resolution VLBI observations. However, we also found that there was not a one-to-one correlation of our classifications with those made from ultradeep X-ray data on the field. The star-forming galaxies agreed well with an extrapolation of a local relation between X-ray luminosity and radio power. In contrast, the AGNs showed a much wider spread in hard X-ray luminosity, including some that had luminosities close to those of the star-forming galaxies. These results suggest that some high-redshift, extremely high star formation

sources may have been incorrectly classified as AGNs if a simple 2 – 8 keV luminosity threshold of 10^{42} erg s $^{-1}$ was used.

We examined the FIR-radio correlation for the classified sources and found that the star-forming galaxies were all within a multiplicative factor of three of the median FIR-radio correlation measured from the star-forming galaxies. However, 5 AGNs also lay within this region. We constructed the SEDs for both the star-forming galaxies and these five AGNs and found that the star-forming galaxies show the characteristic shape of luminous starburst galaxies, while the AGNs show typical torus SEDs and are undetected at wavelengths $\gtrsim 60\ \mu\text{m}$. For these AGNs, we are not measuring SFR from either the FIR luminosity or the radio power, and the fact that they lie on the FIR-radio correlation seems to be mere coincidence. Thus, at least at these high radio powers, one must be cautious in measuring SFRs for radio sources using the FIR-radio correlation without other information available on whether they are AGN dominated or star-formation dominated.

We find that the number of star-forming galaxies drops rapidly above a radio power of $P_{20\ \text{cm}} \approx 5 \times 10^{31}$ erg s $^{-1}$ Hz $^{-1}$. The surface density of these $P_{20\ \text{cm}} > 5 \times 10^{31}$ erg s $^{-1}$ Hz $^{-1}$ sources is about two orders of magnitude lower than that of star-forming galaxies with $P_{20\ \text{cm}} = (1 - 5) \times 10^{31}$ erg s $^{-1}$ Hz $^{-1}$. The 5×10^{31} erg s $^{-1}$ Hz $^{-1}$ bound corresponds to a SFR of just

over a thousand solar masses per year using the Murphy et al. (2011) conversion for a Kroupa (2001) initial mass function.

Finally, since obtaining wide-field, deep submillimeter images is not easy, we used our classifications to investigate whether radio sources could be separated into star-forming galaxies and AGNs based on radio sizes alone. We found that even with the current 20 cm resolution, we were able to put most of the sources into the correct class using a size of 0''.5 as the separation point (i.e., AGNs were smaller than this, and star-forming galaxies were larger). The radio sizes of our submillimeter-detected radio sources are generally larger than those measured for submillimeter-selected galaxies from submillimeter continuum data, but the explanation for this is not yet clear.

We thank the anonymous referee for a careful report that helped us to improve the manuscript. We thank P. Barthel for discussions on the VLBI results. We gratefully acknowledge support from NSF grants AST-1313309 (L. L. C.) and AST-1313150 (A. J. B.), and from the John Simon Memorial Guggenheim Foundation and the Trustees of the William F. Vilas Estate (A. J. B.). The authors wish to recognize and acknowledge the very significant cultural role and reverence that the summit of Maunakea has always had within the indigenous Hawaiian community. We are most fortunate to have the opportunity to conduct observations from this mountain.

REFERENCES

Alexander, D. M., Bauer, F. E., Brandt, W. N., et al. 2003, AJ, 126, 539
 Barger, A. J., Cowie, L. L., Brandt, W. N., et al. 2002, AJ, 124, 1839
 Barger, A. J., Cowie, L. L., Chen, C.-C., et al. 2014, ApJ, 784, 9
 Barger, A. J., Cowie, L. L., Owen, F., et al. 2015, ApJ, 801, 87
 Barger, A. J., Cowie, L. L., & Wang, W.-H. 2007, ApJ, 654, 764
 Barger, A. J., Cowie, L. L., & Wang, W.-H. 2008, ApJ, 689, 687
 Barger, A. J., Wang, W.-H., Cowie, L. L., et al. 2012, ApJ, 761, 89
 Bauer, F., Alexander, D. M., Brandt, W. N., et al. 2004, AJ, 128, 2048
 Bell, E. F. 2003, ApJ, 586, 794
 Best, P. N., & Heckman, T. M. 2012, MNRAS, 421, 1569
 Biggs, A. D., & Ivison, R. J. 2008, MNRAS, 385, 893
 Blain, A. W., Smail, I., Ivison, R. J., Kneib, J.-P., & Frazer, D. T. 2002, PhR, 369, 111
 Bothwell, M. S., Smail, I., Chapman, S. C., et al. 2013, MNRAS, 429, 3047
 Casey, C. M., Narayanan, D., & Cooray, A., 2014, PhR, 541, 45
 Chapin, E. L., Berry, D. S., Gibb, A. G., et al. 2013, MNRAS, 430, 2545
 Chapman, S. C., Smail, I., Windhorst, R., Muxlow, T., & Ivison, R. J. 2004, ApJ, 611, 732
 Chapman, S. C., Blain, A. W., Smail, I., & Ivison, R. J. 2005, ApJ, 622, 772
 Chen, C.-C., Cowie, L. L., Barger, A. J., et al. 2013, ApJ, 776, 131
 Chi, S., Barthel, P. D., & Garrett, M. A. 2013, A&A, 550, 68
 Cohen, J. G., Hogg, D. W., Blandford, R., et al. 2000, ApJ, 538, 29
 Condon, J. J. 1989, ApJ, 338, 13
 Condon, J. J. 1992, AR&A, 30, 575
 Condon, J. J., Kellermann, K. I., Kimball, A. E., Ivezić, Ž., & Perley, R. A. 2013, ApJ, 768, 37
 Cooper, M. C., Aird, J. A., Coil, A. L., et al. 2011, ApJS, 193, 14
 Cowie, L. L., Barger, A. J., Fomalont, E. B., & Capak, P. 2004a, ApJ, 603, L69
 Cowie, L. L., Barger, A. J., & Hu, E. M., Capak, P., & Songaila, A. 2004b, AJ, 127, 3137
 Cowie, L. L., Barger, A. J., Hsu, L.-Y., et al. 2016, ApJ, in press
 Cram, L., Hopkins, A., Mobasher, B., & Rowan-Robinson, M. 1998, ApJ, 507, 155
 Daddi, E., Dannerbauer, H., Krips, M., et al. 2009a, ApJ, 695, L176
 Daddi, E., Dannerbauer, H., Stern, D., et al. 2009b, ApJ, 694, 1517
 de Jong, T., Klein, U., Wielebinski, R., & Wunderlich, E. 1985, A&A, 147, L6
 Del Moro, A., Alexander, D. M., Mullaney, J. R., et al. 2013, A&A, 549, 59
 Dempsey, J. T., Friberg, P., Jenness, T., et al. 2013, MNRAS, 430, 2534
 Elbaz, D., Dickinson, M., Hwang, H. S., et al. 2011, A&A, 533, A119
 Guidetti, D., Bondi, M., Prandoni, I., et al. 2013, MNRAS, 432, 2798
 Helou, G., Soifer, B. T., & Rowan-Robinson, M. 1985, ApJ, 298, L7
 Ho, P. T. P., Moran, J. M., & Lo, K. Y. 2004, ApJ, 616, L1
 Holland, W. S., Bintley, D., Chapin, E. L., et al. 2013, MNRAS, 430, 2513
 Hopkins, A. M., Miller, C. J., Nichol, R. C., et al. 2003, ApJ, 599, 971
 Hornschemeier, A. E., Brandt, W. N., Garmire, G.P., et al. 2001, ApJ, 554, 742
 Ibar, E., Ivison, R. J., Best, P. N., et al. 2010, MNRAS, 401, L53
 Ikarashi, S., Ivison, R. J., Caputi, K. I., et al. 2015, ApJ, 810, 133
 Karim, A., Swinbank, M., Hodge, J., et al. 2013, MNRAS, 432, 2
 Kroupa, P. 2001, MNRAS, 322, 231
 Laird, E. S., Nandra, K., Pope, A., & Scott, D. 2010, MNRAS, 401, 2763
 Larson, D., Dunkley, J., Hinshaw, G., et al. 2011, ApJS, 192, 16
 Lehmer, B. D., Basu-Zych, A. R., Mineo, S., et al. 2016, ApJ, 825, 7
 Mauch, T., & Sadler, E. M. 2007, MNRAS, 375, 931
 Miettinen, O., Novak, M., Smolčić, V., et al. 2015, A&A, 584, 32
 Mineo, S., Gilfanov, M., Lehner, B. D., Morrison, G. E., & Sunyaev, R. 2014, MNRAS, 437, 1698
 Momcheva, I. G., Brammer, G. V., van Dokkum, P. G., et al. 2016, ApJS, 225, 27
 Momjian, E., Wang, W.-H., Knudsen, K. K., et al. 2010, AJ, 139, 1622
 Morić, I., Smolčić, V., Kimball, A., et al. 2010, ApJ, 724, 779
 Morrison, G. E., Owen, F. N., Dickinson, M., Ivison, R. J., & Ibar, E. 2010, ApJS, 188, 178
 Mullaney, J. R., Alexander, D. M., Goulding, A. D., & Hickox, R. C. 2011, MNRAS, 414, 1082
 Murphy, E. J., Condon, J. J., Schinnerer E., et al. 2011, ApJ, 737, 67
 Mushotzky, R. F., Shimizu, T. T., Meléndez, M., & Koss, M. 2014, ApJ, 781, L34
 Muxlow, T. W. B., Richards, A. M. S., Garrington, S. T., et al. 2005, MNRAS, 358, 1159
 Netzer, H., Lutz, D., Schweitzer, M., et al. 2007, ApJ, 666, 806

Pope, A., Borys, C., Scott, D., et al. 2005, MNRAS, 358, 149

Polletta, M., Tajer, M., Maraschi, L., et al. 2007, ApJ, 663, 81

Polletta, M., Wilkes, B. J., Siana, B., et al. 2006, ApJ, 642, 673

Rafferty, D. A., Brandt, W. N., Alexander, D. M., et al. 2011, ApJ, 742, 3

Reddy, N. A., Steidel, C. C., Erb, D. K., Shapley, A. E., & Pettini, M. 2006, ApJ, 653, 1004

Richards, E. A. 2000, ApJ, 533, 611

Sadler, E. M., Jackson, C. A., Cannon, R. D., et al. 2002, MNRAS, 329, 227

Silva, L., Granato, G. L., Bressan, A., & Danese, L. 1998, ApJ, 509, 103

Simpson, J. M., Smail, I., Swinbank, A. M., et al. 2015, ApJ, 799, 81

Swinbank, A. M., Smail, I., Chapman, S. C., Blain, A. W., Ivison, R. J., & Keel, W. C. 2004, ApJ, 617, 64

Symeonidis, M., Giblin, B. M., Page, M. J., et al. 2016, MNRAS, 459, 257

Szokoly, G. P., Bergeron, J., Hasinger, G., et al. 2004, ApJS, 155, 271

Tacconi, L. J., Neri, R., Chapman, S. C., et al. 2006, ApJ, 640, 228

Thomson, A. P., Ivison, R. J., Simpson, J. M., et al. 2014, MNRAS, 442, 577

Trouille, L., Barger, A. J., Cowie, L. L., Yang, Y., & Mushotzky, R. F. 2008, ApJ, 179, 1

Walter, F., Decarli, R., Carilli, C., et al. 2012, Nature, 486, 233

Wirth, G. D., Trump, J. R., Barro, G., et al. 2015, AJ, 150, 153

Wirth, G. D., Willmer, C. N. A., Amico, P., et al. 2004, AJ, 127, 3121

Wong, O. I., Koss, M. J., Schawinski, K., et al. 2016, MNRAS, 460, 1588

Yun, M. S., Reddy, N. A., & Condon, J. J. 2001, ApJ, 554, 803